

3D map of the distribution of metals in a cell: Applications to the toxicity of nanoparticles

Miguel Serras Vasco
miguel.vasco@tecnico.ulisboa.pt

Instituto Superior Técnico, Lisboa, Portugal

April 2016

Abstract

The development of nanoparticle applications have enabled the direct access to biological processes below the cellular scale. However, the full assessment of the biological effects of nanoparticles requires the development of improved imaging techniques. Rutherford Backscattering Spectrometry (RBS), an ion beam analysis technique based on the extraction of sample information from the energy of the back-scattered incident ion, after interacting with a target nucleus, is able to simultaneously identify the elemental matrix of an unknown sample and the depth profile of those elements. While there exists several computational codes available for analysis of RBS spectra, the visualization options of such data are still under-developed. For this thesis, a new computational software was developed, the Micro-beam RBS Image Analyser (MORIA), that enables the presentation of the model of the distribution of a sample element in a 3D environment. MORIA uses the sample matrix, obtained through RBS, and the estimation of the energy loss of the projectile in the sample to calculate the depth of interaction associated to each event, sorted into depth channels, taking into account the effect of the variable Rutherford cross-section and the experimental setup. The validation of the methodology was carried out through analysis of several biological samples exposed to nanoparticles, using ^1H and ^4He ions. For visualization purposes, there are advantages in the use of ^4He ions, concerning a better depth resolution for surface and sub-surface analysis, where as ^1H ions can be used for more global, but less detailed, models.

Keywords: Software, RBS, Microbeam, 3D, Nanoparticles

1. Introduction

The accelerated development of nanotechnology brought a new paradigm to the scope in which the engineering of functional systems were achievable, addressing issues directly at the nanoscale (in the order of $1\text{-}100 \times 10^{-9}\text{m}$). Nanotechnology is now being applied in a multitude of areas, ranging from electronics, chemistry to food and textile production. Yet, the most fascinating application of nanotechnology resides in the biology field.

The cellular biology field presents itself as a natural environment for the development of nanotechnology, due to the scale in which the innumerable cellular functions operate. Nanoparticles (NP), defined as particulate dispersions or solid particles, with a size in the range of 10 to 100 nm, can be used to probe these functions and have tremendous applications in cellular biology research [1] and in the Material and Textile industry[2]. Yet the complete understanding of the biological toxicity of nanoparticles is still unknown [3]. Ongoing research on the biological effects of NP is being carried out, specifically on the quantization, transport, and depth pro-

file of NP in cells, and with that goal in mind high resolution imaging techniques are essential.

The general goal of imaging techniques is to gain a fundamental understanding of the inner structure of matter, which requires the ability to perform the analysis across all length and time scales. However, few are able to combine nanometre probe-formation with precise quantification of the elemental composition of an unknown matrix and the ability to examine the sub-surface layers of a thick sample, retrieving the depth-dependent profile of those elements, as ion beam techniques.

The underlying principles behind many of the different analytical techniques that use ion beams are the same. Initially, a beam of ions, with energy in the order of MeV, is aimed at the target, which will then penetrate the sample, losing energy along their trajectories, at a known rate, through collisions with nuclei and electrons. Due to these interaction, there is a probability, ruled by the respective interaction cross-section, of emission of an output, which can then be detected, collected as a spectra and analysed. This information can give precise details on

the sample's properties, such as atomic structure, matrix composition or elemental depth distribution. One the most commonly used techniques as a material analysis tool is RBS (Rutherford Backscattering Spectrometry), due to its ability to simultaneously give information regarding the sample's elemental structure and the depth profile of its composition, two fundamental properties to fully describe a sample.

1.1. Applications of IB to Biological Studies

Ion beam research on biological samples have been gaining importance, not only due to improvements on the imaging resolution attainable by the experimental setups, but also due to the increased conscience of the influence of nanoscale phenomena, in both biological and biomedical fields. Research using nuclear imaging techniques have been used to examine the biological consequences of the proliferation of NP [4]. More recently, it has been reported [5] that microprobe analysis applied to the identification and quantization of gold NP was able to achieve a 20 nm spatial resolution and obtain direct evidence of the transport mechanism involved in the cellular entry of NP. Using multiple techniques, including RBS, the authors were able to identify the NP, but also to ascertain their depth in the cellular environment with sub-micron resolution, being able to differentiate between NP at the surface of the cell and NPs inside the cell. This technique could allow the determination of the effectiveness of the drug delivery, using a modified gold NP, in terms of distribution and dose, but also enables further studies on the toxicity of NP, a research topic fundamental for a safe widespread use of nanotechnology.

2. Rutherford Backscattering Spectrometry (RBS)

The fundamental basis of RBS is the detection and analysis of the projectile ions which are backscattered, after interacting with the elements that compose the sample's matrix. This allows the identification of the elemental matrix of the sample, and the depth profile of those elements, as a consequence of the elastic collision between the incident ion and the atomic nuclei of the sample matrix, and the energy loss of the ion while transversing the sample, respectively.

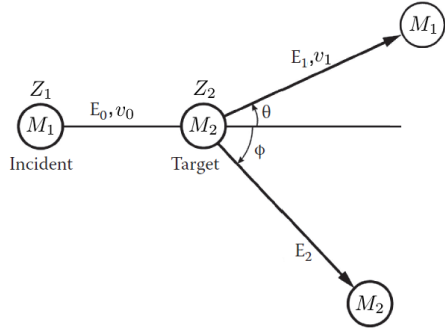


Figure 1: Kinematics of the elastic collision between a projectile particle of mass M_1 , charge Z_1 , and kinetic energy $E_0 = 1/2M_1v_0^2$ and a nucleus at rest of mass M_2 and charge Z_2 . Adapted from [6].

The interaction between the projectile ion and an atomic nuclei of the sample matrix, depicted in Figure 1, can be thought as a two-body elastic collision between isolated particles: when the incident ion, of mass M_1 , charge Z_1 and kinetic energy E_0 , interacts with an target atom at rest, of mass M_2 and charge Z_2 , the ion is scattered through an angle θ , with an atomic recoil angle of ϕ . The ratio of projectile energies after the interaction defines the kinematic factor K_{target} , given by:

$$K_{\text{target}} = \frac{E_1}{E_0} = \left[\frac{[1 - (M_1/M_2)^2 \sin^2 \theta]^{1/2} + M_1/M_2 \cos \theta}{1 + (M_1/M_2)} \right]^2 \quad (1)$$

Hence, for a known ion mass M_1 , the energy loss of the incident ion, after elastically colliding with the target atom, becomes a function only of the scattering angle θ and of the target's mass M_2 and thus the kinematic factor is the fundamental parameter of RBS analysis since, for a fixed θ , given by the detector's angle, it allows a precise identification of the unknown sample element.

However, the interaction of the innumerate ions of the beam with the atoms of the sample's matrix is a statistical process, described as the elastic scattering of charge particles by the Coulomb interaction, giving rise to the Coulomb angular differential scattering cross section, also known as the Rutherford differential cross section which, in the laboratory frame of reference, is given by [6]:

$$\sigma_R = \frac{d\sigma(\theta)}{d\Omega} = \left(\frac{Z_1 Z_2 e^2}{4E} \right)^2 \frac{4}{\sin^4 \theta} \frac{\{[1 - ((M_1/M_2) \sin \theta)^2]^{1/2} + \cos \theta\}^2}{[1 - ((M_1/M_2) \sin \theta)^2]^{1/2}} \quad (2)$$

with θ the scattering angle and E the projectile's kinetic energy. However, the validity of the assumption that the scattering cross-section is purely Rutherford depends on the velocity of the ion, which must be sufficiently large for it to penetrate the inner-most atomic electron orbitals. Indeed, experimental studies have shown to exist a considerable deviation from the Rutherford cross-section at both high and low-energy limits for a proton beam. The low energy deviation is caused by partial screening of the nucleus charge by the inner electrons, thus affecting the value of the Coulomb potential and, subsequently, the value of the scattering cross-section. This screening effect can be taken into account through a correction factor F , such that the screened Rutherford cross-section σ_{SR} is given by:

$$\sigma_{SR} = F\sigma_R \quad (3)$$

Experimental results indicate that the screening correction can be given, with some precision, by the L'Ecuyer factor [7]:

$$F_{L'E} = 1 - \frac{0.049Z_1Z_2^{4/3}}{E_{CM}} \quad (4)$$

where E_{CM} is the center of mass energy (keV), given by:

$$E_{CM} = M_2 \frac{E_0}{M_1 + M_2} \quad (5)$$

with E_0 the energy of the incident beam (keV). The L'Ecuyer factor (4) is a first order correction, that does not take into account the scattering angle θ . In order to acknowledge the angular dependence of the screening in the Rutherford cross-section, the Anderson factor F_A is usually used [8]:

$$F_A = \frac{\left(1 + \frac{1}{2} \frac{V_1}{E_{CM}}\right)^2}{\left(1 + \frac{V_1}{E_{CM}} + \left(\frac{V_1}{2E_{CM} \sin(\theta_{CM}/2)}\right)^2\right)^2} \quad (6)$$

where θ_{CM} is the angle of scattering in the center-of-mass frame and the increase in kinetic energy V_1 (keV) is given by:

$$V_1 = 0.04873Z_1Z_2 \left(Z_1^{2/3} + Z_2^{2/3}\right)^{1/2} \quad (7)$$

However, for large scattering angles ($\theta > 90$) both factors are quite similar and, with increasing energy, their values approach unity. As such, the simpler L'Ecuyer factor is adequate for backscattering cross-section corrections in the low-energy regime. On the other hand, the high-energy deviation to the classical Rutherford scattering is created due to the existence of short-range nuclear forces. While no general theory currently exists to calculate the high-energy departures to the Rutherford cross-section,

according to experimental results conducted by Bozoian, the energy, in the laboratory frame, at which the deviations from the classical Rutherford cross-section are greater than 4% can be determined by experimental relations [9][10]. For a helium ion scattering off a Carbon atom ($Z_2 = 6; M_2 = 12$), the high-energy limit is approximately $E_{CM} = 2$ MeV, corresponding to a beam energy of $E_0 \approx 5.3$ MeV (Equation 5), well above the usual beam energies of 1 to 2 MeV used in RBS analysis, a property shared by all but the lightest of elements. As such, the influence of the high-energy departures of the Rutherford cross-section, for common RBS analysis, will be minor.

The depth profiling ability of RBS is a consequence of the energy loss of the incident ions while transversing the sample before the elastic interaction with an atomic nuclei and after the interaction, before being detected. When an energetic ion traverses a material, it loses energy at a rate dE/dx , named stopping power, usually of a couple of hundred electro-Volt per nanometre, depending on the type of ion projectile (more precisely on M_1 and Z_1) and the elemental matrix of the sample. The energy loss process occurs through successive electronic collisions, in which the projectile's kinetic energy is lost through the excitation and ejection of atomic electrons, and nuclear collisions, where the energy is transferred to kinetic energy to the entire target atom, causing the ion to slow down and, finally, come to rest at some depth in the material. Electronic collisions impart small energy losses and small angle deflections to the ion projectile. On the other hand, nuclear collisions impart large, discrete, energy losses and large angle deflections to the ion projectile. In effect, while being responsible for the backscattered events detected in RBS analysis, nuclear collisions occur quite infrequently due to the nucleus small size, and, as such, for typical ion beam applications, electronic collisions will be the mechanism responsible for most of the projectile's energy loss.

2.1. Depth profile model

Undoubtedly, the most interesting capability of RBS analysis resides in its ability to profile the distribution of elements as a function of its depth. Indeed, it is the loss of energy by the projectile while crossing the medium, characterized by its dE/dx , that enables the extraction of depth information from the sample.

The energy-loss process of ion projectiles occurs in three different stages: first, the ions continuously lose energy through interactions with the electrons of the atoms as they traverse the sample, until elastically colliding with the nucleus of a given element, losing a fraction K_{Target} of its energy, after which the ions, once again, successively lose energy

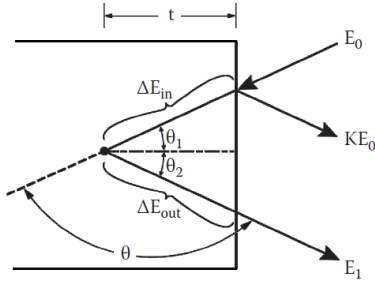


Figure 2: Kinematics of the energy loss mechanism of a beam ion, until its interaction with the nucleus of an element of the sample, at a depth t . Adapted from [11].

through electronic interactions before emerging off the sample. For multi-elemental samples, the energy loss mechanism consists on a sequence of random and independent interactions with atomic electrons. Thus, the stopping cross-section $\epsilon^{A_mB_n}$ of a multi-elemental sample of composition A_mB_n can be determined through Bragg's Law:

$$\epsilon^{A_mB_n} = m\epsilon^A + n\epsilon^B \quad (8)$$

with:

$$\epsilon^{A,B} = \frac{1}{N^{AB}} \frac{dE}{dx_{A,B}} \quad (9)$$

where $dE/dx_{A,B}$ is the stopping power of a given ion in a single-elemental sample of A and B, respectively, and N^{AB} represents the molecular density of the sample. For a given element A, the energy difference at the detector ΔE_A , between an ion scattered at the sample surface and an ion scattered at a depth t , can be given by:

$$\Delta E_A = [\epsilon_A^{AB}] N^{AB} t \quad (10)$$

where the stopping cross-section factor $[\epsilon]_A^{AB}$ is given by

$$[\epsilon]_A^{AB} = \left(K_A \epsilon_{\text{in}}^{AB} \frac{1}{\cos \theta_1} + \epsilon_{\text{out}}^{AB} \frac{1}{\cos \theta_2} \right) \quad (11)$$

where θ_1 and θ_2 are the angles defined in Figure 2 and the stopping powers are those of the ion before and after the interaction with the nucleus. Similar to the mass resolution of the system, it is possible to define depth resolution δt , the minimum detectable difference in depth, related to the minimum energy difference detectable by the experimental apparatus δE , such that:

$$\delta t = \frac{\delta E}{[\epsilon]} \quad (12)$$

Finally, the question of how to evaluate the stopping cross sections arises. For thin films ($t \leq 100$ nm), using commonly ion species for the beam, the relative change in the value of ϵ along the projectile trajectory is small. In other words, the relative

change of the projectile energy is small, and the evaluation can be carried out using the "surface energy approximation", in which ϵ is evaluated at the energy after a elastic collision with a target nucleus at the sample surface, KE_0 :

$$[\epsilon_0] = K_{\text{Target}} \epsilon(E = E_0) \frac{1}{\cos \theta_1} + \epsilon(E = KE_0) \frac{1}{\cos \theta_2} \quad (13)$$

Several examples of computational software exist that are able to analyse, with precision, a given sample using the output of the microbeam setup for the technique. Still, the visualisation of the analysis result does not take fully advantage of the depth capabilities of RBS, more precisely regarding the distribution of elements in a fully 3D-space. In order to tackle this deficiency, a new computational software is needed.

3. The MORIA Software

The development of improved experimental devices for RBS has been closely associated with the development of new computational software that not only enables the extraction of experimental data, but also allows the efficient process of such data, making use of the unique theoretical framework of this technique, along with several others, in ion beam analysis. Still, the visualization options of RBS data are not completely explored, especially concerning the depth information capabilities of the technique.

The MORIA (**M**icro-**R**bs **I**mage **A**nalys**R**) program is a C++ coded software that enables the presentation of the model of the distribution of a given sample element, in a fully 3D environment, and the interaction with the model in real-time. MORIA combines an automated input file processing, with an user-friendly graphical interface, allowing the possibility of setting up the different aspects of the simulation, and a fast, and efficient, 3D renderer.

The MORIA's GUI was designed in wxWidgets, a C++ developed GUI toolkit [12]. Its main advantage is its use of the native platform SDK and of the system-provided widgets. As such, the appearance of the program is a function of the system in which the code was compiled, and compatibility between different systems is guaranteed almost automatically, with little to no code difference. The main disadvantage of this behaviour is the lack of customization on the appearance of the interface of the program, along with the possibility of the existence of platform-specific bugs, due to the code's universality.

The visualization engine is provided by VTK, an open-source cross-platform C++ toolkit, built for 3D modelling, image processing, volume rendering and scientific visualization, with numerous applications in the Biophysics and Radiology field.

The platform-universality of the toolkit, along with its low system requirements, are the main advantages of VTK. The implementation of VTK in the wxWidgets environment is done through wxVTK, a C++ wxWidgets class which enables the rendering and interaction between the two toolkits, such that the visualization engine behaves as another usual wxWidgets component.

3.1. Procedures

The underlying structure of MORIA can be divided into three different processes: file input, data processing and model rendering. The file input procedure aims to recognize a valid input file and the extraction of RBS information from it. The nuclear microprobe facility at CTN uses an Oxford Instrumentation Setup for its data acquisition system, with an complementary analysis software OMDAQ. As such, the allowed input file type of MORIA is the OMDAQ's Listmode (LM) file type (with file extension .LMF), which serves as a collection of event-by-event data, stored in N blocks of information, written by order of detection, due its ability to associate energy values with positions in the sample's 2D-plane. Indeed, each block contains the ADC channel corresponding to the detector where the signal originated, the energy of the event, in a range of 4098 channels, and the beam's X and Y position for each event detected. The file also contains several header blocks at the beginning of the file, responsible for the recording of various types of experimental and formatting information, crucial for subsequent data processing, which are automatically retrieved. In order to enable the analysis and extraction of information from any OMDAQ file in an external application, the OMDAQ Software Development Kit (SDK) was used, which contains the definitions of all the OMDAQ procedures and structures.

The mechanism of file reading in MORIA serves three consecutive goals. The first is the identification of a valid LM file. Subsequently, in the case of a valid LM file, the program extracts information regarding the experimental run directly from the LM file, such as the projectile's charge (Z_1), atomic mass (A_1) and energy (E_0), as well other experimental constrains such as the sample's scan size (ΔS), the detector angle (θ) in the laboratory system, defined in Figure 2, the detector resolution (δE), and the energy calibration of the system, defined by the calibration factors C_0 (keV), C_1 (keV/channel) and C_2 (keV/channel²). Finally, the program stores the multiple RBS events accordingly to their (X,Y) coordinates.

However, due to the usual low number of events in RBS analysis, a sorting taking into account the full range of beam positions (256×256) would result in a

sub-par visualization. As such, the events are stored in an optimal grid dimension of $\Delta G = 64$, combining into a $\Delta G \times \Delta G$ vector of structures, *LMF*, whose initialization, for a given pair of reduced coordinates Xr_i and Yr_i , is presented in Figure 3.1.

```

struct LMF[Xr_i][Yr_i] {
    std::vector<int> X;
    std::vector<int> Y;
    std::vector<float> E;
    std::vector<float> T;
    std::vector<int> Tch;
};

```

Figure 3: Pseudo-code of the initialization of a single instance of the data storage structure in MORIA.

where X is the storage vector of the values of x_i , Y is the storage vector of the values of y_i , E is the storage vectors of the values of energy E_i and T and T_{CH} are the storage vectors of the corresponding depth of the event in nanometres, and in depth channels respectively. The reduced coordinates Xr_i and Yr_i are given by:

$$Xr_i = \left\lfloor x_i \times \frac{256}{\Delta G} \right\rfloor, \quad Yr_i = \left\lfloor y_i \times \frac{256}{\Delta G} \right\rfloor \quad (14)$$

where the floor operator $\lfloor x \rfloor$ refers to the largest integer not greater than x . By default, the energy of each event is stored as a value in a 12-bit range, i.e a value in 4096 channels. However, the calibration stored in the *LM* file is only valid for 1024 channels. As such, the default value of energy is also compressed, using:

$$Er_i = \left\lfloor \frac{E_i}{4} \right\rfloor \quad (15)$$

Thus, the program iterates on the number of events in the event blocks, storing the values (E_i, x_i, y_i) in the corresponding *LMF* structure. After the LM file reading process is finished, it becomes necessary to describe the sample to be analysed as well as the model to be created. More precisely, the user must insert the sample's matrix as well as the analysis limits, such as the element to be modelled, k_{UL} , the element that corresponds to the lower energy limit to be analysed, k_{LL} (whose values of its charge Z_{UL}/Z_{LL} and atomic mass A_{UL}/A_{LL} are automatically assigned from the existent database in the program), and the maximum depth t_M that the analysis should reach. The sample's elemental matrix is given as a sequence of elements k and their correspondent proportion a_k in the matrix, automatically normalized. Through the elemental matrix, the energy loss of the projectile in the sample ϵ , in the inward or the outward path, can be evaluated by the pondered combination of the energy loss

due to each element, in accordance to Bragg's Law (equation 8), taking into account its proportion in the matrix:

$$\epsilon = \sum_k^{N_k} a_k \epsilon^k \quad (16)$$

where ϵ^k refers to the the specific stopping power (keV cm²/g) of each element. The evaluation of each ϵ^k is done using the elemental stopping-power databases from SRIM [13], which are available in text files in the program's installation folder. The discrete values are interpolated using a simple cubic spline interpolation function [14], and ϵ^k is evaluated using the "surface-energy approximation", given in equation 13. Thus, the stopping power is evaluated at two different energies: at the initial beam energy E_0 and at the energy E_1 immediately after the interaction with the nucleus of k_{UL} , given by:

$$E_1 = K_{UL} E_0 \quad (17)$$

where the kinematic factor K_{UL} is given by equation 1. Thus, two different stopping power values emerge: ϵ_{in} , evaluated at E_0 , and ϵ_{out} , evaluated at E_1 . Finally, the stopping power cross-section factor $[\epsilon]_T$ for the sample can be constructed, similar to equation 11:

$$[\epsilon]_T = \left(K_{UL} \epsilon_{in} \frac{1}{\cos \theta_1} + \epsilon_{out} \frac{1}{\cos \theta_2} \right) \quad (18)$$

where $\theta_1 = 0$, $\theta_2 = \theta$, for the CTN's experimental setup, as given in Figure 2. From this quantity, the depth-energy calibration factor t_E (keV/nm) can be determined, given by equation 19

$$t_E = \rho \times [\epsilon]_T \quad (19)$$

where ρ is the matrix density, given by the pondered sum of the densities of e_k , such that:

$$\rho = \sum_k^{N_k} a_k \times \rho_k \quad (20)$$

From this factor, a correspondent depth-channel calibration factor t_{CH} can also be constructed, taking into account the linear energy calibration factor of the system C_1 , such that:

$$t_{CH} = \frac{C_1}{t_E} \quad (21)$$

Another important experimental variable to consider is the depth resolution δt obtainable by the experimental setup. Indeed, using the calibration factor t_E , it is possible to obtain a direct correspondence between the depth resolution and the energy resolution of the detector, given by:

$$\delta t = \frac{\delta E}{t_E} \quad (22)$$

Thus, the maximum number of depth channels available to the analysis is limited by the energy loss of the projectile in the sample. Subsequently, the program determines the upper E_{UL} and lower E_{LL} energy limits for the event sorting, through the surface energy of k_{UL} and k_{LL} , given by:

$$E_{UL} = K_{UL} E_0, \quad E_{LL} = K_{LL} E_0 \quad (23)$$

where K_{LL} refers to the kinematic factor for the element k_{LL} . Thus, the absolute depth t_i of each event i , stored in the bi-dimensional structure $LMF[Xr][Yr].T$, is determined by:

$$t_i = |E_i - E_{UL}| \times t_E \quad (24)$$

where the energy events stored in $LMF[Xr][Yr].E$ were previous calibrated using the calibration factors C_0 , C_1 and C_2 . Afterwards, if the energy of the event is within the limits of analysis given in equation 23, and, if the depth is lower than t_M , the event is stored in the vector T . Due to the existence of a non-null depth resolution δt , the event is also sorted into depth channels t_{CH_i} , of width Δt equal to the depth resolution by default ($\Delta t = \delta t$), which will form the basis of the visualization procedure:

$$t_{CH_i} = \left\lfloor \frac{t_i}{\Delta t} \right\rfloor \quad (25)$$

and the value is stored in the vector T_{CH} . Subsequently, a more manageable 3D vector $Cube[Xr][Yr][Z]$ is created from the LMF structure, with $Z \in [0, t_{CH}^{Max}]$ where t_{CH}^{Max} is the maximum depth channel attained, containing only the number of events at a given position in the 3D space. Finally, in order to better display the distribution of concentration of k_{UL} in the sample, the number of events stored in $Cube[Xr][Yr][Z]$ must be corrected in order to take into account the effect of the increasing Rutherford cross-section with increasing depth in the sample, as discussed in Section 2, using the L'Eculyer factor:

$$Cube[Xr][Yr][Z]_C = \frac{F_{L'E}^{E=E_0} \sigma_R^{t=0}}{F_{L'E}^{E=\Delta E_i} \sigma_R^{t=\delta t \times Z}} \times Cube[Xr][Yr][Z] \quad (26)$$

where $\sigma_R^{t=0}$, $\sigma_R^{t=\delta t \times Z}$ are calculated using equation 2 and $F_{L'E}^{E=E_0}$, $F_{L'E}^{E=\Delta E_i}$ are calculated using equation 4, respectively evaluated at energy E_0 and ΔE_i , which takes into account the energy loss of the projectile up to the interaction depth, i.e.:

$$\Delta E_i = E_0 - t_i \times t_E; \quad (27)$$

Finally, the 3D model of the distribution of k_{UL} in the sample can be created. The model of a

given element in MORIA is composed of a 3D vector of *vtkCubeSource* source data objects in number equal to the number of non-null entries in *Cube[Xr][Yr][Z]*. In order to correctly represent the sample, the X_{Cube} and Y_{Cube} dimensions (surface plane) of each *vtkCubeSource* object are to be taken accordingly with the scan size of the experimental run and the Z_{Cube} dimension is magnified by a multiplicative factor of 10, to minimize the difference between the magnitudes of the surface plane dimensions and the depth dimension, such that:

$$\begin{aligned} X_{\text{Cube}} &= Y_{\text{Cube}} = \frac{\Delta S}{\Delta G}, \\ Z_{\text{Cube}} &= \delta t \times 10 \end{aligned} \quad (28)$$

The information regarding the number of events in each element of the model is given through color mapping. Hence, given an entry in the 3D-vector *Cube[X][Y][Z]*, with n_{ev} events, the [R,G,B] code of the associated *vtkPolyData*[X_{Cube}][Y_{Cube}][Z_{Cube}] surface, a data object which stores color information, is given by [15]:

$$\begin{aligned} R &= \max(0, (3 - |\delta - 4| - |\delta - 5|)/2) \\ G &= \max(0, (4 - |\delta - 2| - |\delta - 4|)/2) \\ B &= \max(0, (3 - |\delta - 1| - |\delta - 2|)/2) \end{aligned} \quad (29)$$

where $\delta = 4.4 \times n'_i - n'_i$ and n'_i corresponds to the mapping of n_{ev} to the interval $[0, 1]$. In order to reduce the computational complexity of rendering a large number of independent elements, a *vtkAppendPolyData* filter was used, which is able to append the full set of individual *vtkPolyData* objects into a single global *vtkPolyData* model, at the cost of losing the ability to interact individually with each model. In order to remove duplicate points and degenerate cells in the *vtkAppendPolyData* output model, resulting from the attachment of the individual cells, a *vtkCleanPolyData* filter was subsequently used in the visualization pipeline. Afterwards, the program uses the standard chain of objects for VTK visualization, consisting of a *vtkPolyDataMapper*, a subclass object of *vtkMapper* responsible for mapping the source object into the *vtkActor* object, responsible for the physical manifestations of the data, which is subsequently added to *VTKRenderer*, responsible for displaying the actor object in a real-time 3D environment.

4. Applications of MORIA to Biological Samples

In order to validate the model, different applications of MORIA are presented, regarding the creation of 3D models of the depth distribution of nanoparticles in biological samples: copper oxide nanoparticles (CuO-NP) in *Saccharomyces cerevisiae* (Chap-

Table 1: Point RBS spectrum matrix, concerning the *S. cerevisiae* organisms, using ^1H and ^4He beams.

Beam species	Matrix
^1H	C(3.01)N(0.5)O(1.1)Cu(0.45) K(0.8)Na(0.48)P(0.11)
^4He	C(3)O(1.2)N(1)Cu(0.18) Cl(0.05)K(0.05)P(0.05)

Table 2: Results of the SC_1 model analysis, obtained using MORIA

Parameter	^1H beam	^4He beam
t_{E} (keV/nm)	0.061	0.590
$t_{\text{CH}}^{\text{Max}}$	4	11
t^{Max} (nm)	1011	340

ter 4.1) and in *Nematodes* (Chapter 4.2), and Au-NP in *HeLa* cells (Chapter 4.3).

4.1. *Saccharomyces cerevisiae*

The analysis of *Saccharomyces cerevisiae* samples exposed to a concentration of 40 mg/L of 20 nm copper oxide nanoparticles (CuO-NP), using the microbeam facility available at CTN, applying both ^1H and ^4He ion beams, is presented in order to assess the potential of each ion type for imaging purposes.

The proton-beam analysed sample SC_1 is a $26 \times 26 \mu\text{m}^2$ scan, containing two individual diploid *Saccharomyces cerevisiae* organisms: one in the top-left most area of the scan ($\text{SC}_{1,1}$) and another in the bottom right area of the scan ($\text{SC}_{1,2}$). On the other hand, the helium-beam analysed sample SC_2 is a $26 \times 26 \mu\text{m}^2$ scan, containing a single individual diploid *Saccharomyces cerevisiae* cell.

To construct the model of the distribution of the CuO-NPs in the samples, it becomes necessary to determine the composition each cell's biological matrix. In order to minimize the contribution of the polycarbonate backing, over which the samples are prepared, the matrices were determined using the simulation and fit of a single point RBS spectra, for each sample, in OMDAQ, representative of the cell: $\text{SC}_{1,C}$ and $\text{SC}_{2,C}$, whose matrices are presented in Table 1.

Finally, the results of the model analysis of the SC_1 and SC_2 samples in MORIA are presented in Table 2.

The cross-section of the distribution of Cu in the $\text{SC}_{1,1}$ cell, presented in Figure 4, reveals the non-uniformity of the distribution of NP in the cellular environment which could indicate the presence of cellular organelles which are not as permeable

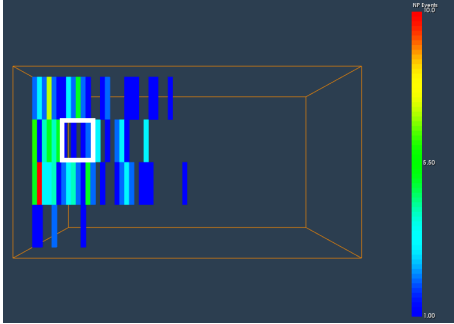


Figure 4: Cut of the 3D distribution of copper in the $SC_{1,1}$ cell, highlighting a volume in the cell with decrease NP concentration.

to CuO-NP as the cellular wall. Assuming that the volume of the unknown component is also comprised of 7 *blocks* of length in the direction perpendicular to the render of Figure 4, the unknown component has a volume $V \approx 3.53 \mu\text{m}^3$, similar to the volume of the nucleus of a *S. cerevisiae* cell ($V_{\text{Nuc}} \approx 4.22 \mu\text{m}^3$), thus implying the impermeability of the nucleus to CuO-NP. However further research with longer acquisition times and a higher resolution beam, along with the usage of complementary imaging techniques are needed to fully ascertain the identification.

The cross-section of the distribution of Cu in the SC_2 cell is presented in Figure 5 with 3 depth channels, each with approximately 110 nm of length. Once again, this SC_2 cell seems to have assimilated a considerable amount of CuO-NP, although the more superficial distribution seems to indicate that a fewer concentration of these nanoparticles are actually inside the cell in comparison with the SC_1 case. This uniformity is notable in the first depth channel ($\Delta t = 110$ nm), hinting at a considerable level of surface accumulation of NP aggregates due to some degree of impermeability of the cellular wall of *S. cerevisiae* cells. However, at deeper levels in the cell, the spatial distribution of NP in the cell seems to be non-homogeneous, which could give new insight into the issue of the NP entry mechanism in *S. cerevisiae*, currently unresolved [16].

4.2. Nematode

The nematode sample N_1 analysis aims to gauge the efficiency of the methodology for thicker samples, using a ^4He beam. The sample contains an *nematode*, whose typical thickness ranges from 5-100 μm . Analogously to the previous analysis, the biological matrix of the sample was obtained through spectrum simulation and fit to the experimental RBS spectrum of a single point representative of the nematode, in OMDAQ, presented in Table 3.

The results of the model analysis of the N_1 sample in MORIA are presented in Table 4.



Figure 5: Cut of the 3D distribution of copper in the SC_2 cell, with only 3 depth channels.

Table 3: Point RBS spectrum matrix concerning the *nematode* organisms, using ^4He beam.

Beam species	Matrix
^4He	C(600)N(68.79)O(25.62) Cu(1.5)K(1)Cl(1)P(1)

Table 4: Results of the N_1 model analysis, obtained using MORIA

Parameter	^4He beam
t_E (keV/nm)	0.634
$t_{\text{CH}}^{\text{Max}}$	10
t^{Max} (nm)	316

The low maximum depth obtained by the methodology, $t^{\text{Max}} = 316$ nm, confirms the difficulty of attaining a more global model of the distribution of CuO-NPs in the case of thicker samples. However, the analysis can still provide valuable information regarding the surface and sub-surface distribution of these nanoparticles in a *nematode*, which is presented in Figure 6.

As expected from the low concentration of Cu in the sample matrix, the low number of events are not able to completely cover the intestine of the nematode, which along with the considerable number of CuO-NP events distributed randomly outside the body of the animal and the fact of the beam can only probe the surface layers of the sample, contribute to a difficult model to analyse. This low number of CuO-NP events in the body of the animal can be attributed to a low intake of the nematode to this type of nanoparticles or to a high expelling rate of CuO-NP off its body. The first hypothesis seems to be preferred since, as seen in Figure 6, the majority of events occur in the most superficial layer of the sample, and thus were not assimilated by the nematode.

4.3. HeLa cell

The final analysis concerns the 3D model distribution of Gold nanoparticles (AuNP) in a sample of

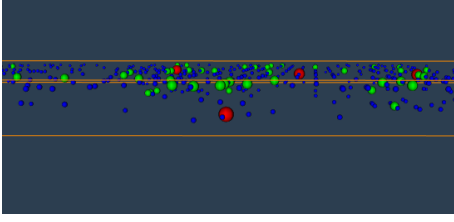


Figure 6: Depth distribution of copper in the N_1 cell, using the MORIA's *sphereview* function, with 3 depth channels.

HeLa cells (HL_1) conducted in the Centre for Ion Beam Applications at the National University of Singapore (CIBA@NUS), which used a 300 nm spot size ^4He beam and whose output file was kindly provided by the group. Due to the impossibility of obtaining a single point spectrum, after conversion to a valid LM file, the biological matrix of the sample was obtained through spectrum simulation and fit to the experimental RBS spectrum of an area mask of the sample representative of the cell. The obtained matrix is presented in Table 5:

Table 5: Area mask RBS spectrum matrix concerning the *HeLa* cell, using ^4He beam.

Beam species	Matrix
^4He	C(2.4)O(0.62)N(1.18) Na(0.06)P(0.03)Au(0.01)

Finally, the results of the model analysis of HL_1 sample in MORIA are presented in Table 6.

Table 6: Results of the HL_1 model analysis, obtained using MORIA

Parameter	^4He beam
t_E (keV/nm)	0.502
t_{CH}^{Max}	23
t^{Max} (nm)	892

The distribution of these nanoparticles in the *HeLa* sample is presented in Figure 7.

The distribution of AuNP across the cell, whose contour can be seen in Figure 7, does not seem homogeneous, but occurring in discrete agglomerates. As such, the discrete agglomerates of nanoparticles in the cell are consistent with their mechanism of entry in the cellular space by endocytosis, by being enclosed in endosomal vesicles [17]. Moreover, the model created can effectively achieve the same result of a color scaling to translate depth information in a fully 3D environment, as seen by the correct identification and correspondence of the AuNP agglomerates in Figure 8, serving as a validation of

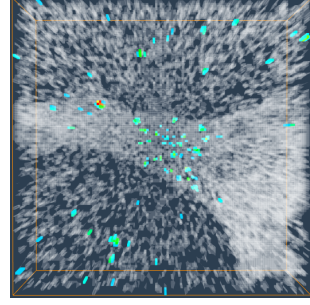


Figure 7: 3D distribution of Au in the HL_1 cell, along with the auxiliary model with a Na(O,1) matrix, created using the Surface model of the HL_1 sample, highlighting the contour of the *HeLa* cell, with 5 depth channels.

the methodology.

5. Conclusions

The advent and the subsequent rapid development of nanotechnology has led to its dissemination across a multitude of scientific and industrial fields, leading to the necessity for improved imaging techniques, which are simultaneously able not only to spatially differentiate individual agglomerates but also to retrieve the depth profile of such agglomerates, in order to assess their biological danger.

The core focus of this article was the presentation a new tool, the MORIA program, which could be able to display the 3D distribution of a chosen element in the sample's space and interact, in real-time, with the created model. While the program is functional, future updates of the program must address some inadequacies in its methodology, more precisely calculation of the energy loss in the sample, which currently resorts to the "surface-energy approximation", whose validity for samples with thickness over 1 μm can be argued, and improved memory management.

For validation of the program's methodology, several biological samples were analysed, using different beam species. The choice of the beam species becomes a function of the purpose of the analysis: the inspection of surface and sub-surface sample volumes with high depth resolution, in the order of tens of nanometres, using ^4He ions, or a more global analysis of the distribution of a given element in the sample, using ^1H ions. Still, the analysis in MORIA was able to give new insights into the distributions of nanoparticles in cells, as discussed in Section 4.

The necessity for improved imaging techniques is only expected to increase in the near future, and with it the necessity for improved experimental methodologies and analytical techniques. RBS, due to its maturity in the material analysis field and precision of its results, can also be recognized as a

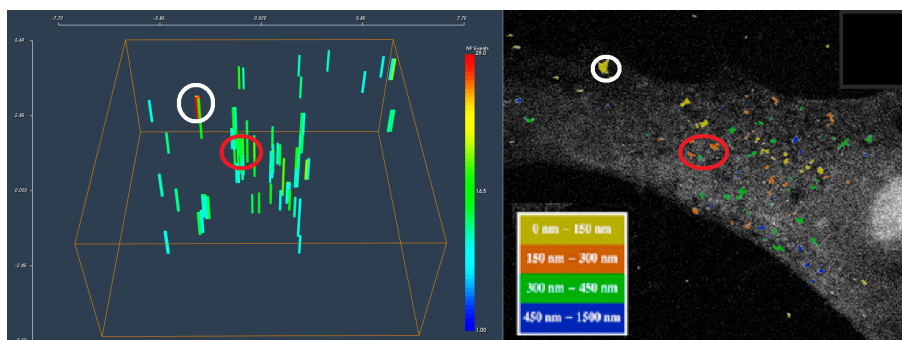


Figure 8: Secondary view of the 3D distribution of Au in the sample, with 5 depth channel, highlighting the different depths at which the AuNP exist in the sample along with the distribution of the AuNP in the HeLa cell, with color information regarding its depth (adapted from [5]), which allows the correspondence of the nanoparticle agglomerates in both images.

powerful imaging technique, especially taking into account its ability to probe not only the surface but also the sub-surface of biological samples. At the same time, the ever-changing nature of a computational program such as MORIA allows for the implementation of improvements, many of which already discussed, in future updates, in order to construct a more complete and useful scientific tool. Thus, hopefully, the real value of the work presented will lie in its purpose in scientific research and, hopefully, in its assistance in the never-ending development of improved imaging techniques.

References

- [1] VJ Mohanraj and Y Chen. Nanoparticles - a review. *Tropical Journal of Pharmaceutical Research*, 2006.
- [2] Ali Sedighi, Majid Montazer, and Nahid Hemmatinejad. Copper nanoparticles on bleached cotton fabric: in situ synthesis and characterization. *Cellulose*, 21(3):2119–2132, 2014.
- [3] Ya-Nan Chang, Mingyi Zhang, Lin Xia, Jun Zhang, and Gengmei Xing. The toxic effects and mechanisms of cuo and zno nanoparticles. *Materials*, 5(12):2850–2871, 2012.
- [4] Rita M. Godinho, Maria Teresa Cabrita, Luis C. Alves, and Teresa Pinheiro. Imaging of intracellular metal partitioning in marine diatoms exposed to metal pollution: consequences to cellular toxicity and metal fate in the environment. *Metallomics*, 6(9):1626, 2014.
- [5] Xiao Chen, Ce-Belle Chen, Chammika Udalagama, N.B., Minqin Ren, Kah Ee Fong, Lin Yue Lanry Yung, Pastorin Giorgia, Andrew Anthony Bettiol, and Frank Watt. High-resolution 3d imaging and quantification of gold nanoparticles in a whole cell using scanning transmission ion microscopy. *Biophysical Journal*, 104(7):1419–1425, 2013.
- [6] Michael Nastasi, James W Mayer, and Yongqiang Wang. *Ion beam analysis: fundamentals and applications*. CRC Press, 2014.
- [7] J. L’Ecuyer, J.A. Davies, and N. Matsunami. How accurate are absolute rutherford backscattering yields. *Nuclear Instruments and Methods*, 160(2):337–346, 1979.
- [8] H. H. Andersen, F. Besenbacher, P. Loftager, and W. Moller. Large-angle scattering of light ions in the weakly screened rutherford region. *Phys. Rev. A*, 21(6):1891–1901, 1980.
- [9] Michael Bozoian, Kevin M. Hubbard, and Michael Nastasi. Deviations from rutherford-scattering cross sections. *Nuclear Instruments and Methods in Physics Research Section B: Beam Interactions with Materials and Atoms*, 51(4):311–319, 1990.
- [10] Michael Bozoian. Deviations from rutherford backscattering for $z = 1, 2$ projectiles. *Nuclear Instruments and Methods in Physics Research Section B: Beam Interactions with Materials and Atoms*, 58(2):127–131, 1991.
- [11] Yongqiang Wang. *Handbook of modern ion beam materials analysis*. Materials Research Society, 2009.
- [12] Julian Smart, Kevin Hock, and Stefan Csomor. *Cross-platform GUI programming with wxWidgets*.
- [13] J. F Ziegler, J. P Biersack, and Matthias D Ziegler. *SRIM, the stopping and range of ions in matter*. SRIM Co., 2008.
- [14] Tino Kluge. *c++ cubic spline interpolation library*, 2016.
- [15] Alexandru C Telea. *Data Visualization*. CRC Press, 2014.
- [16] Sana Thabet, France Simonet, Marc Lemaire, Chantal Guillard, and Pascale Cotton. Impact of photocatalysis on fungal cells: depiction of cellular and molecular effects on *saccharomyces cerevisiae*. *Applied and environmental microbiology*, 80(24):7527–7535, 2014.
- [17] Tore-Geir Iversen, Tore Skotland, and Kirsten Sandvig. Endocytosis and intracellular transport of nanoparticles: present knowledge and need for future studies. *Nano Today*, 6(2):176–185, 2011.